Published in final edited form as:
Phys Med Biol. 2014 February 21; 59(4): 925–949. doi:10.1088/0031-9155/59/4/925.

MAP Reconstruction for Fourier Rebinned TOF-PET Data

Bing Bai[1], **Yanguang Lin**[2], **Wentao Zhu**[2], **Ran Ren**[2], **Quanzheng Li**[3], **Magnus Dahlbom**[4], **Frank DiFilippo**[5], and **Richard M. Leahy**[2]

Richard M. Leahy: leahy@sipi.usc.edu

[1]Department of Radiology, University of Southern California, Los Angeles, CA 90033, U.S.A

[2]Signal and Image Processing Institute, University of Southern California, Los Angeles, CA 90089, U.S.A

[3]Department of Radiology, Harvard Medical School/MGH, Boston, MA 02114, U.S.A

[4]Department of Molecular and Medical Pharmacology, University of California, Los Angeles, CA 90095, U.S.A

[5]Department of Nuclear Medicine, Cleveland Clinic Main Campus, Cleveland, OH 44195, U.S.A

Abstract

Time-of-flight (TOF) information improves signal to noise ratio in Positron Emission Tomography (PET). Computation cost in processing TOF-PET sinograms is substantially higher than for nonTOF data because the data in each line of response is divided among multiple time of flight bins. This additional cost has motivated research into methods for rebinning TOF data into lower dimensional representations that exploit redundancies inherent in TOF data. We have previously developed approximate Fourier methods that rebin TOF data into either 3D nonTOF or 2D nonTOF formats. We refer to these methods respectively as FORET-3D and FORET-2D. Here we describe maximum a posteriori (MAP) estimators for use with FORET rebinned data. We first derive approximate expressions for the variance of the rebinned data. We then use these results to rescale the data so that the variance and mean are approximately equal allowing us to use the Poisson likelihood model for MAP reconstruction. MAP reconstruction from these rebinned data uses a system matrix in which the detector response model accounts for the effects of rebinning. Using these methods we compare performance of FORET-2D and 3D with TOF and nonTOF reconstructions using phantom and clinical data. Our phantom results show a small loss in contrast recovery at matched noise levels using FORET compared to reconstruction from the original TOF data. Clinical examples show FORET images that are qualitatively similar to those obtained from the original TOF-PET data but a small increase in variance at matched resolution. Reconstruction time is reduced by a factor of 5 and 30 using FORET3D+MAP and FORET2D+MAP respectively compared to 3D TOF MAP, which makes these methods attractive for clinical applications.

1. Introduction

Positron emission tomography (PET) is a useful molecular imaging modality which provides quantitative and non-invasive information about biochemical and physiological processes (Ollinger & Fessler 1997). Over the last two decades, image quality has improved greatly thanks to advancements in instrumentation and data processing methods including the development of new detectors and advanced electronics, the evolution of three-dimensional (3D) PET systems and the new information gained by the use of time-of-flight (TOF) technology (Conti et al. 2005). In TOF-PET, the difference between the arrival times at the detectors of the two photons is measured, which can be used to help identify the location of positron/electron annihilation along the line connecting the two detectors. Although the idea of using TOF in PET was suggested as early as the 1960s (Anger 1966) and PET scanners

with TOF capability were built decades ago (Gariod et al. 1982, Yamamoto et al. 1982, Wong et al. 1983), TOF-PET scanners for clinical use only became available recently, when faster detectors and better electronics made it possible to exploit TOF information in clinical applications (Moses & Derenzo 1999). Given the current timing resolution of a few hundred picoseconds, TOF-PET has little effect on the spatial resolution of the image. However by incorporating the TOF information in image reconstruction, the signal-to-noise ratio (SNR) of the image can be substantially improved (Tomitani 1981, Watson 2007, Vunckx et al. 2010). It has been found that the SNR improvement is proportional to the ratio between subject size and timing resolution. Phantom and patient studies have confirmed that incorporating TOF information in image reconstruction leads to better image quality and provides benefits in clinical patient studies (Karp et al. 2008, Kadrmas et al. 2009, El Fakhri et al. 2011).

Iterative reconstruction methods such as ordered-subsets expectation maximization (OSEM) and maximum a posteriori (MAP) have been widely used in PET image reconstruction and provide superior image quality compared to analytical methods (Defrise et al. 1994, Chatziioannou et al. 2000, Frese et al. 2003). However the computational cost of these methods is high due to the large number of lines of response (LORs) collected for each data set. TOF adds yet one more dimension and increases the size of the dataset by a factor of 10 to 20 with current timing resolutions. The most time-consuming part of the iterative reconstruction algorithm is forward and back projection. In order to reduce reconstruction time, one can design fast projector pairs (Hong et al. 2007) or use specialized hardware such as graphic processing units (Pratx et al. 2009, Zhou & Qi 2011, Lin et al. 2010).

Listmode reconstruction has been investigated for TOF PET (Wang et al. 2006) and can be an efficient approach to processing of high dimensional data. However an advantage of sinogram-based reconstruction is that fast projector/backprojector pairs can be developed by exploiting geometric symmetries and sparseness of the system matrix leading to shorter reconstruction times (Qi et al. 1998a, Hong et al. 2007). Consequently, for clinical TOF-PET scanners, reconstruction from histogrammed data is still widely used.

Another way to reduce data size and computational cost is to exploit the redundancy in the data. For fully 3D PET, Fourier Rebinning (FORE) rebins nonTOF 3D PET sinograms into a set of stacked 2D sinograms (Defrise et al. 1994). For noiseless data, the rebinned data is equivalent to the 2D data, while for noisy data the rebinned data has improved SNR relative to directly measured 2D data. Similar algorithms have also been designed for TOF-PET data (Defrise et al. 2005, Cho et al. 2009). We have derived a pair of Fourier rebinning methods for TOF data (FORET) that convert TOF sinograms to either 2D or 3D nonTOF sinograms while retaining the SNR advantages of the TOF information (Cho et al. 2009). We also developed an optimal weighting scheme for rebinning TOF into nonTOF data and showed that under reasonable approximations it is the best linear unbiased estimator (Ahn et al. 2011). In this paper, we investigate the application of FORET-3D, which rebins 3D TOF data to 3D nonTOF data, and FORET-2D, which rebins 3D TOF to 2D nonTOF data, to phantom and human data from a clinical TOF PET scanner.

After the data is rebinned, an iterative reconstruction algorithm such as OSEM or MAP can be used to reconstruct the image (Kinahan et al. 1996). These iterative algorithms with an accurate system model have been successfully used for some time to generate PET images in clinical and preclinical studies. We have previously shown that MAP can be used to reconstruct FORET rebinned data (Cho et al. 2009, Ahn et al. 2011). Here we develop an optimized FORET+MAP reconstruction method for clinical data. Our MAP algorithm assumes that the data are independent Poisson random variables. For the Poisson distribution the mean of the data is equal to the variance. This is no longer the case after rebinning

because rebinning reduces variance. To reconstruct images from this rebinned data, we can either develop an estimator with a noise model that matches that of the rebinned data, or continue to use a Poisson model but rescale the rebinned data so that its mean and variance are matched. We use this latter approach inspired by the earlier work of (Comtat et al. 1998) and (Liu et al. 2001) who combined Fourier rebinning of nonTOF data with OSEM reconstruction. We first develop an approximate variance model for FORET rebinned data that accounts for the effects of randoms and scatter correction, rebinning and arc correction. Using this we find rescaling factors to approximately match mean and variance. We then apply MAP reconstruction methods to the scaled rebinned data.

The MAP reconstruction used here is based on a factored system model (Qi et al. 1998a, Lin et al. 2010). This system model accounts for the effects of block detector design using a Monte Carlo simulation that models the path of photons through the block, accounting for gaps between the block, inter-crystal scatter and crystal penetration. FORET results in additional blurring in the sinogram. Below we describe an iterative approach to estimating the effective sinogram blur kernels from simulated point sources that explicitly model sinogram blurring in the rebinned data (Lin et al. 2013). A similar approach has previously been described for FORE rebinned nonTOF data (Tohme & Qi 2010). Although FORET ignores the detector response model, by assuming that the detector response is locally approximately shift invariant, we can assume that the detector response effects are reflected in the rebinned as well as in the original data. We therefore use this detector response model when recosnstructing from FORET rebinned data. Our MAP algorithm also includes a data-dependent smoothing term to ensure approximately count independent resolution (Fessler & Rogers 1996).

We evaluate the quality of FORET+MAP images using phantom and patient scans. We use the scaling method described above and data dependent smoothing for count independent resolution. We first compute resolution calibration curves as a function of global smoothing parameter β for each of the reconstruction methods. We then compute MAP reconstructions at matched resolution for FORET rebinned as well as TOF and nonTOF MAP reconstructions. We compare performance in terms of contrast recovery and noise performance in a phantom study. Finally a wholebody patient example is included to demonstrate image quality for clinical data.

2. Notation

In this paper, we use the following notation:

- Matrices are denoted using bold capital letters, e.g. **P**.
- Vectors are denoted using bold lower case letters, e.g. **y**.
- P_{ij} or $P(i, j)$ is the $(i, j)^{th}$ element of **P** and y_i or $y(i)$ the i^{th} element of **y**.
- A Fourier transform (FT) of the data is denoted by calligraphic capital letters, e.g. $\mathcal{P}(\omega_s, \varphi, z, \delta; \omega_t)$ where ω_s, ω_t are the frequency variables corresponding to s and t respectively.
- We use superscripts to denote the data format, for example, $\mathbf{p}^{TOF}$ represents 3D TOF data. To refer generally to data that may have more than one format, e.g. 3D nonTOF, 2D nonTOF or 3D TOF, we drop the superscript. A similar notational convention is used for the system matrices, **P**.

3. Fourier Rebinning of TOF Data

We denote a 3D object by $f(x, y, z)$. The 3D TOF PET data from a cylindrical scanner can be expressed as

$$p(s,\phi,z,\delta;t)=\sqrt{1+\delta^2}\int_{-\infty}^{\infty} f(s\cos\phi-l\sin\phi, s\sin\phi+l\cos\phi, z+l\delta)h(t-l\sqrt{1+\delta^2})\,dl \quad (1)$$

where s and φ are the radial and angular coordinates, respectively, z is the axial midpoint of each line of response (LOR), δ is the tangent of the oblique angle θ, t is the TOF variable, and h represents the one dimensional (1D) TOF kernel. (Cho et al. 2009) developed a unified framework for Fourier Rebinning of TOF-PET data based on the generalized projection slice theorem

$$\mathcal{P}(\omega_s,\phi,\omega_z,\delta;\omega_t)=\sqrt{1+\delta^2}\mathcal{H}(\omega_t)\mathcal{F}(\omega_s\cos\phi-\chi\sin\phi, \omega_s\sin\phi+\chi\cos\phi, \omega_z) \quad (2)$$

where $\mathcal{P}(\omega_s, \varphi, \omega_z, \delta; \omega_t)$ is the 3D FT (Fourier transform) of $p(s, \varphi, z, \delta; t)$ with respect to s, z, t with ω_s, ω_z and ω_t the corresponding frequency variables. $\mathcal{F}(\omega_x, \omega_y, \omega_z)$ is the 3D FT of the image, $\mathcal{H}(\omega_t)$ is the 1D FT of the TOF kernel, and $\chi=\omega_t\sqrt{1+\delta^2}-\delta\omega_z$.

There is no unique solution to ($\omega_s \cos\varphi - \chi \sin\varphi = \omega_x$, $\omega_s \sin\varphi + \chi\cos\varphi = \omega_y$) for each ($\omega_x$, ω_y) because of redundancy in the 3D TOF data. As a consequence we can develop many different rebinning schemes that map from 3D TOF data to a lower dimensional representation. (Cho et al. 2009) describe two approximate rebinnings that map to 3D nonTOF data (FORET-3D) and 2D nonTOF data (FORET-2D). FORET-3D uses the relationship:

$$\mathcal{P}_{3D}(\omega_s,\phi,z,\delta;0)\approx\frac{\mathcal{H}(0)}{\mathcal{H}(\omega_t)}\mathcal{P}_{3D}(\omega_s',\phi',z,\delta;\omega_t) \quad (3)$$

where $\mathcal{P}_{3D}(\omega_s, \varphi, z, \delta; \omega_t)$ is the 2D FT of $p(s, \varphi, z, \delta; t)$ with respect to s and t. $\omega_s'=\omega_s\sqrt{1-(\omega_t\sqrt{1+\delta^2}/\omega_s)^2}$ and $\phi'=\phi-\arctan(\omega_t\sqrt{1+\delta^2}/\omega_s')$. FORET-2D uses the following approximate relationship:

$$\mathcal{P}_{2D}(\omega_s,k,z,0;0)\approx\frac{1}{\sqrt{1+\delta^2}}\frac{\mathcal{H}(0)}{\mathcal{H}(\omega_t)}\exp\left(-ik\frac{\omega_t\sqrt{1+\delta^2}}{\omega_s}\right)\mathcal{P}_{2D}(\omega_s',k,z+\frac{\delta k}{\omega_s},\delta;\omega_t) \quad (4)$$

$\mathcal{P}_{2D}(\omega_s, k, z, \delta; \omega_t)$ is the 3D FT of $p(s, \varphi, z, \delta; t)$ with respect to s, φ and t, and k is the frequency index corresponding to φ. Note that while (Cho et al. 2009) used the approximation $\omega_s' \approx \omega_s$ for FORET-2D so only a 1D interpolation is needed in z', here we use the more accurate approximation $\omega_s'=\omega_s\sqrt{1-(\omega_t\sqrt{1+\delta^2}/\omega_s)^2}$, which requires a 2D interpolation in (ω_s', z'). We found that the FORET-2D images were more accurate with this approximation and the additional computation is negligible.

In FORET-3D, the 1D FT of the 3D nonTOF data in s is estimated by taking a weighted average over ω_t of the 2D FT of TOF sinograms in s and t. Similarly in FORET-2D, the 2D FT of the 2D nonTOF data in s and φ is estimated by a weighted average over both ω_t and

oblique angle δ of the 3D FT of the TOF data in s, φ and t. We can express the FORET-3D rebinning process as:

$$\mathscr{P}_{3D}(\omega_s,\phi,z,\delta;0)=\frac{\sum_{\omega_t:\omega_s^2>\omega_t^2(1+\delta)}\alpha(\omega_t)\frac{\mathscr{H}(0)}{\mathscr{H}(\omega_t)}\mathscr{P}_{3D}(\omega_s',\phi',z,\delta;\omega_t)}{\sum_{\omega_t:\omega_s^2>\omega_t^2(1+\delta)}\alpha(\omega_t)} \quad (5)$$

and FORET-2D as:

$$\mathscr{P}_{2D}(\omega_s,k,z,0;0)=\frac{\sum_{\omega_t}\alpha(\omega_t)\sum_{\delta}\frac{\mathscr{H}(0)}{\mathscr{H}(\omega_t)}\frac{1}{\sqrt{1+\delta^2}}\exp(-ik\frac{\omega_t\sqrt{1+\delta^2}}{\omega_s})\mathscr{P}_{2D}(\omega_s',k,z',\delta;\omega_t)}{\sum_{\omega_t}\sum_{\delta}\alpha(\omega_t)} \quad (6)$$

where $z'=z+\frac{\delta k}{\omega_s}$. Note that in the discretized FORET calculations, interpolation is needed because ω_s', ϕ', z' may fall between sample points. The nonnegative weights $\alpha(\omega_t)$ play an important role in determining the SNR of the rebinned sinograms. (Ahn et al. 2011) showed that for FORET-3D, the best linear unbiased estimator is approximately achieved when $\alpha(\omega_t) = \mathcal{H}^2(\omega_t)$. We use this weighting here for both FORET-3D and 2D. Finally, after the data are rebinned a bow-tie filter is applied to ensure the consistency of the data (Cho et al. 2008).

4. MAP Reconstruction for FORET Rebinned TOF Data

4.1. A 3D TOF-PET Data Model

The reconstruction methods we use here are based on a stored system matrix originally described in (Qi et al. 1998a) and recently applied to TOF-PET reconstruction in (Lin et al. 2010). The measured TOF-PET data $\mathbf{y}^{TOF}$ can be modeled as independent Poisson random variables with mean and variance given by:

$$\bar{\mathbf{y}}^{TOF}=var(\mathbf{y}^{TOF})=\mathbf{P}^{TOF}\mathbf{x}+\bar{\mathbf{r}}^{TOF}+\bar{\mathbf{s}}^{TOF} \quad (7)$$

where $\mathbf{x}$ is the 3D tracer distribution or image, and $\bar{\mathbf{y}}^{TOF}$, $\mathbf{r}^{TOF}$ and $\mathbf{s}^{TOF}$ are the means of the prompt, random and scattered events in the 3D TOF data respectively; $var(\mathbf{y}^{TOF})$ is a vector representing the variance for each LOR. $\mathbf{P}^{TOF}$ is the system matrix which can be written as:

$$\mathbf{P}^{TOF}=\mathbf{P}_{norm}^{TOF}\mathbf{P}_{blur}^{TOF}\mathbf{P}_{attn}^{TOF}\mathbf{P}_{geom}^{TOF} \quad (8)$$

where $\mathbf{P}_{geom}^{TOF}$ is the geometric projection matrix for TOF data, which is based on a solid angle calculation (Qi et al. 1998a, Lin et al. 2010) with sensitivities for each voxel weighted by the TOF kernel. $\mathbf{P}_{norm}^{TOF}$ and $\mathbf{P}_{attn}^{TOF}$ are the diagonal normalization and attenuation matrices. $\mathbf{P}_{blur}^{TOF}$ operates on the data in sinogram space to model block detect response as a local blurring. One component of the normalization $\mathbf{P}_{norm}^{TOF}$ is caused by the block structure and referred to as an interference pattern (Casey et al. 1995). This same factor is modeled in the blur kernels $\mathbf{P}_{blur}^{TOF}$ as described in our earlier work (Qi et al. 1998b). To ensure consistency of the model in 8 when using the standard (vendor supplied) normalization, we normalize the blur kernel matrix $\mathbf{P}_{blur}^{TOF}$ so that $\mathbf{P}_{blur}^{TOF}\mathbf{1} = \mathbf{1}$ where $\mathbf{1}$ is a vector of ones. These matrices for TOF data are related to their nonTOF versions by

$$\begin{aligned}\mathbf{P}_{norm}^{TOF}&=\mathbf{I}_{N_t}\otimes\mathbf{P}_{norm}^{3D}\\ \mathbf{P}_{attn}^{TOF}&=\mathbf{I}_{N_t}\otimes\mathbf{P}_{attn}^{3D}\\ \mathbf{P}_{blur}^{TOF}&=\mathbf{I}_{N_t}\otimes\mathbf{P}_{blur}^{3D}\end{aligned}\quad(9)$$

where $\mathbf{I}_{N_t}$ is an $N_t \times N_t$ identity matrix, N_t is the number of TOF bins, and $\otimes$ represents the Kronecker product. In the following we will compare MAP reconstructions based on this model, with 2D and 3D MAP reconstructions of the rebinned data.

4.2. Noise Properties of FORET Rebinned Data

To account for the discrepancies between the line integral implicit in the rebinning method and the accurate system model above, we need to perform a sequence of operations on the data as illustrated in Figure 1, first to convert to a form suitable for FORET rebinning, and then back to a form that can be combined with MAP reconstruction of the 2D or 3D nonTOF data.

We first subtract estimates of randoms and scatter to obtain an estimate of the true coincidences. We then resample this data uniformly in *s*, the radial coordinate. This arc correction compensates for the inherent nonuniform sampling that arises naturally because of the circular arrangement of the detectors around the patient. The data is then rebinned to 2D or 3D nonTOF formats. Since we will reconstruct the image using MAP based on the above system model, we then reverse the arc correction step, referred to here as "un-arc correction". Finally, we perform an affine transform on the rebinned data to ensure that its noise variance approximately matches its mean. We do this because the MAP reconstruction methods are based on a Poisson model and rescaling the rebinned data produces a quasi-Poisson distribution (mean=variance).

An alternative approach to reconstruction is to use a weighted least squares (WLS) method as described for rebinned nonTOF data in (Alessio et al. 2007). The appropriate weighting is the inverse of the covariance matrix. Rebinning introduces correlation and estimation of the non-diagonal inverse covariance is difficult and time consuming. An alternative is to use a diagonal weighting matrix with elements equal to the reciprocal of the variances of each sinogram element. To investigate the impact of ignoring correlations, we include the following simulation in which we explore whether using diagonal WLS is preferable to unweighted LS in cases where the off-diagonal components of the covariance are not estimated.

We assume $\mathbf{x} = (x_1, x_2)'$ is a 2×1 random vector with independent components x_1 and x_2. $\mathbf{y}$ is a 3×1 random vector related to $\mathbf{x}$ by $\mathbf{y} = A\mathbf{x}$, where A is a 3×2 matrix. We solve the WLS problem with a diagonal matrix composed of the inverse of the variance of data. We also solve the unweighted LS problem. The covariance of the solutions obtained using both methods can be derived analytically given A. We generated a large number of random matrices A and for each computed the variance of the estimated *x*'s using LS and diagonal WLS. Figure 2 shows a histogram of the ratio of LS to WLS variance. While on average, diagonal WLS results in a smaller variance that LS (i.e. the ratio greater than one) in some cases, unweighted LS can perform better (ratio less than one). Based on this observation, we would also expect that reweighting rebinned data to match mean and variance will, on average, lead to improved performance when reconstructing using MAP with a Poisson likelihood model compared to the case where we apply the same method directly to the rebinned data. This is because the Poisson model ignores correlation in a similar manner to the diagonal WLS method. Approximations to the covariance matrix that do take local

correlations into account have been derived for FORE rebinned nonTOF data by (Alessio et al. 2007). However the results obtained show only marginal improvements in image quality.

Based on the simulation above and the results from (Alessio et al. 2007), it appears that there are advantages to reweighting the data to match mean and variance and furthermore, that incorporating simplified models of the noise correlation structure into the estimator will lead to only minor additional improvements. However we note with reference to Figure 2 that there could be cases where reweighting produces inferior results relative to the unweighted case. In section 5.4 we use a more realistic Monte Carlo simulation to further compare the relative performance of MAP with unweighted and reweighted data.

The FORET rebinned data after un-arc correction in Figure 1 can be written as

$$\mathbf{y}_{unarc}^{FORET}=\mathbf{M}_{unarc}\mathbf{R}\mathbf{M}_{arc}\mathbf{P}_{norm}^{TOF-1}\mathbf{P}_{attn}^{TOF-1}(\mathbf{y}^{TOF}-\bar{\mathbf{r}}^{TOF}-\bar{\mathbf{s}}^{TOF}) \quad (10)$$

where $\mathbf{y}_{unarc}^{FORET}$ represents the unarc corrected 2D or 3D nonTOF data prior to the final affine transform step. $\mathbf{M}_{arc}$ and $\mathbf{M}_{unarc}$ are two matrices representing the arc and un-arc corrections and $\mathbf{R}$ is the matrix representing FORET rebinning; $\mathbf{r}^{TOF}$ and $\mathbf{s}^{TOF}$ are the estimated mean random and scattered sinograms. In the latest generation of clinical PET scanners, corrections make use of CT based attenuation, component based normalization, model based scatter calculation and estimated randoms. Negligible additional noise is introduced by these factors compared to that in the data itself and here we assume that mean randoms and scatter as well as the calibration factors are known deterministic quantities.

The experimental results presented in the next section are acquired on the Siemens mCT clinical TOF PET scanner. The design of this scanner leaves a gap of approximately one detector width between blocks. The resulting gaps in the sinograms can be accounted for in the system model used with MAP reconstruction. However, the gaps need to be filled before applying Fourier rebinning since these methods assume uniform sampling of the sinogram. We accomplish this using the same approach we use for arc correction, i.e. linear interpolation between adjacent samples across the gap. The effect of gap filling can therefore be included as part of the arc correction model, $\mathbf{M}_{arc}$.

The mean of the rebinned data is

$$\bar{\mathbf{y}}_{unarc}^{FORET} \approx \mathbf{M}_{unarc}\mathbf{R}\mathbf{M}_{arc}\mathbf{P}_{blur}^{TOF}\mathbf{P}_{gcom}^{TOF}\mathbf{x} \quad (11)$$

Note that equation (11) assumes $\mathbf{P}_{blur}^{TOF}\mathbf{P}_{attn}^{TOF} \approx \mathbf{P}_{attn}^{TOF}\mathbf{P}_{blur}^{TOF}$. Since sinogram blurring is a local operation and attenuation correction factors are generally smooth, this is a reasonable approximation.

The final step before reconstruction is to apply an affine transform to the data so that mean and variance are matched. In the Appendix we derive approximate expressions for variance of the rebinned 3D and 2D data. These expressions can be written in the general form (44), repeated here for convenience:

$$var(\mathbf{y}_{unarc}^{FORET})=\mathbf{G}\bar{\mathbf{y}}_{unarc}^{FORET}+\mathbf{L}(\bar{\mathbf{r}}^{3D}+\bar{\mathbf{s}}^{3D}) \quad (12)$$

where $\bar{\mathbf{y}}_{unarc}^{FORET}$ is the mean of the un-arc corrected 2D or 3D FORET rebinned data and $\mathbf{r}^{3D}$ and $\mathbf{s}^{3D}$ are respectively the 3D estimates of randoms and scatters. $\mathbf{G}$ and $\mathbf{L}$ are respectively matrices combining all terms that result from the effect of applying the operator defined in

(11) to the corrected data, which results in the propagation of variance in the trues, scatters and randoms into the final rebinned variance.

The affine transformed data can be written as:

$$\mathbf{y}^{LT}=\mathbf{D}_1\mathbf{y}^{FORET}_{unarc}+\mathbf{d}_2 \quad (13)$$

where $\mathbf{D}_1$ is a diagonal matric and $\mathbf{d}_2$ a vector. Using (12), we have:

$$\begin{aligned} var(\mathbf{y}^{LT}) &= \mathbf{D}_1^2 var(\mathbf{y}^{FORET}_{unarc}) \\ &= \mathbf{D}_1^2\mathbf{G}\bar{\mathbf{y}}^{FORET}_{unarc}+\mathbf{D}_1^2\mathbf{L}(\bar{\mathbf{r}}^{3D}+\bar{\mathbf{s}}^{3D}) \end{aligned} \quad (14)$$

Comparing equations (13) and (14), we see that the mean and variance of the transformed data are equal when

$$\begin{aligned} \mathbf{D}_1 &= \mathbf{G}^{-1} \\ \mathbf{d}_2 &= \mathbf{G}^{-2}\mathbf{L}(\bar{\mathbf{r}}^{3D}+\bar{\mathbf{s}}^{3D}) \end{aligned} \quad (15)$$

This affine transformation is applied to the rebinned data prior to MAP reconstruction. The Poisson likelihood function used in the MAP optimization is then based on the model for the mean of the data:

$$\bar{\mathbf{y}}^{LT}=\mathbf{D}_1\bar{\mathbf{y}}^{FORET}_{unarc}+\mathbf{d}_2=\mathbf{D}_1\mathbf{P}_{blur}\mathbf{P}_{geom}\mathbf{x}+\mathbf{d}_2 \quad (16)$$

where $\mathbf{P}_{blur}$ contains the detector response blurring kernels and $\mathbf{P}_{geom}$ represents the 3D or 2D geometric projection matrix for FORET-3D and FORET-2D respectively.

4.3. System Modeling for FORET Rebinned PET Data

We reconstruct images from the FORET rebinned data using a MAP algorithm with a system model that incorporates a detector response blurring kernel. The approach used to compute the blur kernel for a 3D PET system is to use Monte Carlo simulations to track the paths of multiple photon pairs through the detectors. This method was originally described in (Qi et al. 1998a). The Monte Carlo code tracks the path of photons through the crystals in the block modeling the effects of crystal penetration and intercrystal scatter and accounts for the gaps of approximately one detector width between detector blocks as found inOur code models the Siemens mCT scanner (Siemens Molecular Imaging, Knoxville, TN). To account for these gaps, we introduce a virtual crystal between blocks with zero probability of stopping or scattering the photon. In this way we can model the effect of photons entering the side of the edge crystals in the block. The resulting kernels are appropriate for use with directly acquired TOF or nonTOF PET data.

For FORET rebinned data, there is additional blurring due to the rebinning prodecure. We compute the effective, local blurring kernel for FORET-3D using an iterative procedure from point source data in a manner similar to that of (Tohme & Qi 2010). We use an expectation maximization (EM) algorithm as follows (Lin et al. 2013): Suppose we have N point sources and $\mathbf{b}$ is a vector containing all elements of the blur kernel matrix $\mathbf{P}_{blur}$, then:

$$\boldsymbol{Y}^{FORET}_{unarc}=\boldsymbol{Y}_{geom}\mathbf{b} \quad (17)$$

where $\mathbf{Y}_{geom}$ is an $(N_s \times N) \times N_b$ matrix composed of the elements of the nonTOF forward projection of the point source data using $\mathbf{P}_{geom}$ (the geometric projection matrix only) and

$\boldsymbol{Y}_{unarc}^{FORET}$ is a vector size ($N_s \times N$), that contains the FORET rebinned point source data. N_s is the number of elements in the rebinned sinogram and N_b is the dimension of b, the total number of nonzero elements in the blur kernel. In this model we assume that the blur kernels are dependent on the relative position of the detectors within the blocks, but exploit the symmetry with respect to the blocks themselves. The EM update equation is:

$$\mathbf{b}^{\mathrm{m}+1}=\mathbf{b}^{\mathrm{m}}.*(\boldsymbol{Y}_{geom}^{'}(\boldsymbol{Y}_{unarc}^{FORET}./(\boldsymbol{Y}_{geom}\mathbf{b}^{\mathrm{m}}))))./(\boldsymbol{Y}_{geom}^{'}\mathbf{1}) \quad (18)$$

where .* and ./ are element wise multiplication and division, **1** is a vector of ones.

We estimate the FORET-3D blur kernels from simulated point source data. Because of the symmetry across detector blocks, it is sufficient to place the point sources on a narrow band that covers one detector block along the radial direction. A total of 1326 point sources were used in our simulation.

Figure 3 shows examples of the estimated FORET-3D blur kernel. Figure 4 shows profiles of the projection of point sources. Without blur kernels, the point source nonTOF sinograms do not reflect the increased blurring towards the edge of the field of view. However, when we apply the new blur kernels to the nonTOF sinograms the shape matches the variable resolution seen in the FORET-3D rebinned sinograms from TOF data that includes the original blur kernels. In other words, the new blur kernels are consistent with the blurring seen in FORET-3D rebinned data.

FORET-2D introduces additional axial blurring which we have not studied. For now we assume FORET-2D and FORET-3D share the same transverse blurring within sinogram and apply our estimated FORET-3D blur kernel to FORET-2D rebinned data.

4.4. Count Independent Resolution

It is well known that MAP reconstruction with a shift invariant smoothing or penalty function will have count dependent resolution (Fessler & Rogers 1996). To achieve approximately count independent resolution we use spatially variant smoothing (Qi & Leahy 2000):

$$\beta\mathbf{U}(x)=\frac{1}{2}\beta\sum_{j=1}^{N}\sum_{k\in N_j,k>j}q_{jk}\hat{\kappa}_j\hat{\kappa}_k(x_j-x_k)^2 \quad (19)$$

where q_{jk} is the reciprocal of the Euclidean distance between the j^{th} and k^{th} voxels and $\hat{\kappa_j}$ and $\hat{\kappa_k}$ are the j^{th} and k^{th} diagonal elements of the estimated Fisher information matrix $\mathbf{F}=\mathbf{P}^{'}D(1/\overline{y_i})\mathbf{P}$. Here $\bar{y}_i$ is the mean of the i^{th} element of the sinogram and **P** is the system matrix. N is the number of sinogram elements; N_j is the set that contains all the neighbors of the j^{th} voxel; β is a global smoothing parameter. Note that this calculation can be applied to any of the data formats: original 3D TOF, FORET-2D or FORET-3D provided that the rebinned data are first rescaled so that they follow a psuedo-Poisson distribution.

Using this approach we can achieve approximately count invariant resolution. We computed calibration curves of FWHM resolution vs global smoothing parameter β for reconstructions from each of the three data formats. To do this we use the approximation that the mean of the reconstructed image equals the reconstruction obtained from the mean of the data (Fessler & Rogers 1996). A series of reconstructions of the mean of the original (for TOF MAP) or rebinned (for FORET-2D and FORET-3D MAP) data are computed for a point source in a uniform backgroud. From these we compute the FWHM as a function of β to produce the calibration curves (Li et al. 2009). In the comparisons presented below, we are

then able to show images from the three different data formats at approximately matched spatial resolution.

5. Results

5.1. Computation Time

The major motivation for developing FORET rebinning is to reduce the computation time. Table 1 compares the computation time for the FORET operations and different reconstruction methods on a Linux workstation with two 2.53 GHz Intel Xeon E5630 Quad processors and 24 GB of RAM. The code is not fully optimized but is equivalent across the three different data types (TOF, FORET-2D and FORET-3D). Times are for 621 sinograms size 400x168 and reconstruction on a 256 x 256 by 111 slice voxel volume. The reconstruction time can be reduced through further optimization or use of GPUs (Lin et al. 2010). We typically run one iterations of OSEM followed by 20 iterations of MAP. Since the objective function is convex in MAP optimization, the solution is not sensitive to the initial image. We use one iteration of OSEM to reduce the number of MAP iterations required to reach effective convergence. Compared to 3D-TOF MAP, 3D nonTOF and 2D nonTOF MAP can reduce the reconstruction time by a factor of 5 and 30 respectively.

5.2. Variance Estimation for FORET Rebinned Data

In this section, we use a Monte Carlo simulation to evaluate the accuracy of our variance model for FORET rebinned sinograms. We simulated the geometry of the Siemens mCT TOF PET scanner (Jakoby et al. 2011). Simulation parameters are shown in Table 2. We selected the image for one bed position extracted from a whole-body patient study and smoothed with a 5mm Gaussian filter. We then forward projected the smoothed image using the full system model to create noiseless 3D TOF sinograms (Lin et al. 2010). We used the randoms and scatters calculated from the scanner software for this dataset as the mean of randoms and scatters. The normalization and attenuation correction files from the patient data were also used in the simulation. We then generated 100 datasets from this mean data set using a Poisson random number generator.

To process the data we first corrected using the mean of randoms and scatters and the normalization and attenuation correction files. We then applied arc correction, FORET-3D and FORET-2D rebinning, and finally un-arc correction. We computed the sample variances for these corrected data and compared with the values calculated using (12). Figure 5 shows profiles of the sample variance from the Monte Carlo simulation and theoretical computation from (12) for FORET-3D and FORET-2D. While there is still residual Monte Carlo variability in the variance estimates, it is clear that for both 2D and 3D rebinning, the variances are approximately correct. We note that in the tails where the signal and variance are both small, our approximation underestimates the variance. We believe that this is primarily because of the approximations described in the Appendix. To prevent this causing problems with incorrect scaling factors for LORs at the boundary of the patient, we use the attenuation correction factors (ACF) to identify these LORs. We set the scale factor to unity for LORs in which ACF < 1.05. To look at these relationships from a more general perspective, Figure 6 shows histograms of the ratio of variance to mean of the data after the affine transform using (13) at which point the mean and variances should be equal. These plots show the distribution after truncation of scale factors to unity for LORs with ACF < 1.05. In both cases the ratios have their mode very close to unity. The long tails on these distributions reflect the regions in the sinogram corresponding to low activity in which the variance is underestimated. We see that modification of the scale factors based on the ACFs as described above does not fully control this problem, but note that the variance ratio will always be bought closer to unity than is the case before scaling.

Figure 7 compares the different variance approximations developed in the Appendix for the estimated FORET-2D variance for the same line of the sinogram as in Fig. 5. The blue curve is the variance calculated from Monte Carlo simulations. The red curve shows the estimated variance from (39) which uses single slice rebinning of the FORET-2D data to compute variance. The black curve implements (43) in which the single slice rebinning is replaced by calculations based directly on the FORET-2D data. The green curve also uses (43) but in addition simplifies the computation of variance contribution from scatters and randoms. Rather than using the single slice rebinning in (40), these factors are caculated directly from FORET-2D rebinning of randoms and scatters. These results show that (43) is a reasonably good approximation to (39) provided the randoms and scatter contributions are caculated using the more complex single slice rebinning formula (40). Further simplification of the randoms and scatter contributions lead to larger errors in the overall estimated variance. Consequently, we proceed with a comparison of FORET-2D and FORET-3D based on the scaling in (44).

Figure 8 shows the variance reduction factor $K_{F2D}(z)$ (see Appendix, (35)) in comparison to the mean sample variance reduction factor in each sinogram calculated from Monte Carlo simulations. The reduction factor reflects the combination of averaging over both time of flight and the oblique angles. As a result, noise reduction is largest in the central slice of the scanner, which has the maximum number of oblique sinograms that contribute when rebinning. The plots show good correspondence between Monte Carlo and theoretical calculations except at the outermost planes, again supporting the use of the scaling described in Section 4.2 to match the variance to the mean.

5.3. Resolution vs. β Calibration

To compute the resolution vs. β calibration curves we simulated a line source in a uniform cylindrical phantom with low background activity (ratio 300:1). The reconstruction voxel size was 2mm. We reconstructed images for different values of β for TOF, nonTOF, FORET-3D and FORET-2D algorithms. Results are shown in Figure 9. These curves clearly show that dependence on β varies with processing method. The FORET-3D and FORET-2D curves are almost the same as are the TOF and nonTOF curves. It can also be seen that the resolution of nonTOF and TOF images are higher than FORET-3D and FORET-2D with the same β value. The additional blurring of FORET degrades the image resolution slightly. The highest resolution achieved by TOF is 4.6mm, nonTOF is 4.7mm while FORET-3D and FORET-2D are both 5.7mm. Interestingly, the FORET-3D and nonTOF 3D curves are almost the same. This is probably as a result of the scaling we perform to match mean and variance which results in the curves depending primarily on the data format. Note that as we reduce dimensionality from 3D TOF to 3D nonTOF (either through FORET-3D or summing over TOF bins) to 2D nonTOF (through FORET-2D), larger values of β are required to meet a given resolution for the lower resolution portion of the curves. At higher resolutions the 3D and 2D nonTOF curves cross. At these higher resolutions it is possible that the different approximations as a function of rebinning scheme have a larger impact on resolution resulting in the cross over of the curves.

5.4. Comparison of Reconstruction from Scaled and Unscaled Data

To investigate the impact of using the quasi-Poisson noise model of rebinned data, we simulated a lung phantom with five point sources scanned in a 2D TOF PET system. The geometry of this 2D system is based on one detector ring of the Siemens mCT scanner. Noisy TOF data was generated using an independent Poisson random number generator. The mean total number of counts simulated was 1 million. First the data were rebinned using FORET-3D applied to the single transaxial TOF sinogram, we then rescaled the data and reconstructed using the quasi-Poisson model. For this 2D case we were able to compute the

exact variance of the rebinned data using knowledge of the mean of the data. We also reconstructed the FORET rebinned data without rescaling. Figure 10 shows the true phantom and reconstructed images at three different resolutions with and without sinogram rescaling. While similar, the results with reweighting appear superior in terms of noise propagation. To investivate this further we computed resolution vs. noise curves as shown in Figure 11. Each resolution vs. noise curve here and later was obtained by reconstructing the data with different β values. In Figure 11(a), the background noise was calculated as an ensemble statistic across Monte Carlo trials using the mean region of interest (ROI) activity, while in Figure 11(b), the background noise was calculated using the variance of the voxels within a single ROI. Figure 11(a) clearly shows the advantage of using rescaling while Figure 11(b) shows inconclusive results. This is because Figure 11(b) underestimates background variance due to correlation across the ROI. We have included both figures here as a likely explanation of the apparent discrepancy we see between the earlier simulations summarized in Figure 2 which show clear advantages of rescaling, and our later results (see Section 5.5) which show similar results with and without scaling.

5.5. Phantom Measurements

Reconstructed image quality was evaluated using an anthropomorphic torso phantom with breast attachments. The phantom was filled with ^{18}F-FDG and scanned for 10 minutes on a Siemens mCT scanner. The phantom has liver and myocardium compartments and two lesions represented using hot spheres with 15.8 mm diameter inserted in the abdominal region. The relative activity in the torso background, liver, myocardium and lesions was 1:1.91:3.85:3.85. The images reconstructed from 3D TOF data, 3D nonTOF, FORET-3D and FORET-2D data are shown in Figure 12. An 8mm diameter ROI was drawn in the center of one of the hot spheres and a 20mm diameter spherical ROI drawn in the body. We measured the contrast recovery coefficient (CRC) using the following equation

$$CRC=(\overline{f}_{hot}-\overline{f}_{bkg})/(a-1) \quad (20)$$

where $\overline{f}_{hot}$ and $\overline{f}_{bkg}$ are the average values of the voxels in the hot ROI and background ROI respectively; a is the true activity ratio (a = 3.85). The images in Figure 12 have matched CRC of 0.8. The CRC vs. noise result is shown in Figure 13. It can be seen that the TOF images have the best quality, with lower noise at the same contrast recovery level, while FORET-3D and FORET-2D result in some loss of contrast at matched noise levels, but still noticeably better than the nonTOF reconstructions. Figure 14 compares the CRC vs. noise properties of the FORET-3D and FORET-2D images. The curves show that inclusion of the detector response model improves image quality significantly, while the scaling sometime result in apparently worse results compared to unscaled results. As we noted earlier, this could be caused by two factors: First we are not considering the correlation of the data and second as we have shown in section 5.4, computing background variance in an ROI in a single image leads to sensitivity to correlation, so that variance is increasingly underestimated as noise correlation increases resulting in misleading CRC vs. noise curves. The FORET-2D image also shows artifacts which may arise from the less accurate approximation used in FORET-2D than in FORET-3D. We also reconstructed the FORET data without the affine transform for variance matching and without blur kernels. This clearly shows worse performance than all other methods and indicates the importance of response modeling and variance scaling.

5.6. Whole-body Patient Data

To illustrate the relative performance of the rebinning methods in clinical studies we applied all four reconstruction methods to a clinical whole-body scan collected using the Siemens

mCT scanner. The patient was a 66-year-old female, weighting 85.7kg. 451 MBq of ^{18}F-FDG was injected and the scan started 46 minutes after injection. The patient was scanned using a standard clinical protocol, with six bed positions and three minutes per bed. The data were reconstructed using TOF MAP, nonTOF MAP and FORET+MAP. The smoothing parameter β was selected such that the resolution of the reconstruct image was 6mm. In all cases we initialized with one iteration of OSEM followed by 20 iterations of MAP to ensure effective convergence. Coronal sections through these images are shown in Figure 15.

An ROI was drawn in the liver and we measured the noise in the image calculated as the voxel-to-voxel percent standard deviation (SD) in the ROI. The result is shown in Table 3. Results in the Table reflect the visual appearance shown in Figure 15. With FORET-3D having slightly larger SD than TOF, FORET-2D clearly worse, and nonTOF the largest SD. Similar performance was seen in other clinical studies comparing these methods.

6. Discussion and Conclusion

We have applied MAP reconstruction to Fourier rebinned TOF-PET data. We developed a noise model for the FORET rebinned data, and used this as the basis for an affine transform such that the transformed data are approximately Poisson. A new blur kernel was estimated from simulated FORET rebinned point source data so that the blurring effects of rebinning are also included in the reconstruction model. Monte Carlo simulation results show that the variance calculations, although with several approximations, are reasonably accurate. Phantom studies confirmed that inclusion of the blur kernels improved image quality significantly. However, somewhat surprisingly, the beneficial impacts of rescaling to match variance are marginal. Our simulation studies indicate that there should be some improvement from rescaling, but the impact in phantom studies is small, indeed in the FORET-2D case, numerical performance was better for the unscaled data. As noted above, this can be partly explained by the bias in computing regional variance from a single ROI. With reference to Figure 10 we see that rescaling does tend to produce reduced anisotropy in the noise correlation structure but at the expense of some increase in anisotropy in the local impulse response. While the method described in Section 4.4 is able to enforce approximately count-independent resolution, this approach does not control the shape of the local impulse response. Using a more complicated asymmetric weighting in the regularizer (Stayman & Fessler 2000, Fessler 2003) could address this problem. A distinct advantage to rescaling, in combination with spatially variant smoothing, is that is possible to compute calibration curves so that images reconstructed using any of the four formats considered here (TOF, FORET-3D, FORET-2D, nonTOF) can be reconstructed at known count-independent resolution.

Our results show a clear progression in quality from TOF through FORET-3D, FORET-2D and finally nonTOF. This is clear in both the phantom and clinical examples. While the ordering is unsurprising, we expected that the FORET results, particularly for 3D, would be closer in quality to TOF than they are. Our basis for this assumption is that our earlier results in (Ahn et al. 2011) indicated that there was little information loss in FORET rebinning. The cause of the somewhat worse than expected performance for FORET may be due to two main factors: (i) errors in the approximations assumed in the FORET rebinning equations and (ii) the use of the blur kernel optimized for data that has not been rebinned. Another possible factor affecting FORET image quality is correlation introduced into the rebinned data which we do not account for in the scaling process described here. Despite these issues however, the FORET rebinned images still retain much of the advantage of TOF data in comparison to nonTOF data and show little qualitative difference in the final clinical example. The reconstruction time of FORET3D+MAP and FORET2D+MAP is reduced by a factor of 5 and 30 respectively when compared to 3D TOF MAP. The saving of

computation time makes it attractive to reconstruct high quality images using FORET+MAP from TOF-PET data for routine clinical studies.

Acknowledgments

The authors thank Michael E. Casey, Vladimir Panin and Christian Michel of Siemens Medical Solutions for their assistance in working with data from Siemens mCT scanner. This work was supported by NIH grant no. R01 EB010197.

References

Ahn S, Cho S, Li Q, Lin Y, Leahy R. Optimal rebinning of time-of-flight pet data. Medical Imaging, IEEE Transactions on. 2011; 30(10):1808–1818.

Alessio A, Sauer K, Kinahan P. Statistical image reconstruction from correlated data with applications to pet. Physics in Medicine and Biology. 2007; 52:6133–6150. [PubMed: 17921576]

Anger, H. Technical report. Univ. of California; Berkeley: 1966. Survey of radioisotope cameras.

Casey, ME.; Gadagkar, H.; Newport, D. A component based method for normalization in volume pet. 3rd Int. Meeting on Fully Three-Dimensional Image Reconstruction in Radiology and Nuclear Medicine; IEEE; 1995. p. 67-71.

Chatziioannou A, Qi J, Moore A, Annala A, Nguyen K, Leahy R, Cherry S. Comparison of 3-d maximum a posteriori and filtered backprojection algorithms for high-resolution animal imaging with micropet. Medical Imaging, IEEE Transactions on. 2000; 19(5):507–512.

Cho S, Ahn S, Li Q, Leahy RM. Analytical properties of time-of-flight pet data. Physics in Medicine and Biology. 2008; 53(11):2809. URL: http://stacks.iop.org/0031-9155/53/i=11/a=004. [PubMed: 18460746]

Cho S, Ahn S, Li Q, Leahy RM. Exact and approximate fourier rebinning of pet data from time-of-flight to non time-of-flight. Physics in Medicine and Biology. 2009; 54(3):467. URL: http://stacks.iop.org/0031-9155/54/i=3/a=001. [PubMed: 19124956]

Comtat C, Kinahan P, Defrise M, Michel C, Townsend D. Fast reconstruction of 3d pet data with accurate statistical modeling. Nuclear Science, IEEE Transactions on. 1998; 45(3):1083–1089.

Conti M, Bendriem B, Casey M, Chen M, Kehren F, Michel C, Panin V. First experimental results of time-of-flight reconstruction on an lso pet scanner. Physics in Medicine and Biology. 2005; 50(19): 4507. URL: http://stacks.iop.org/0031-9155/50/i=19/a=006. [PubMed: 16177486]

Defrise M, Casey ME, Michel C, Conti M. Fourier rebinning of time-of-flight pet data. Physics in Medicine and Biology. 2005; 50(12):2749. URL: http://stacks.iop.org/0031-9155/50/i=12/a=002. [PubMed: 15930600]

Defrise M, Geissbuhler A, Townsend DW. A performance study of 3d reconstruction algorithms for positron emission tomography. Physics in Medicine and Biology. 1994; 39(3):305. URL: http://stacks.iop.org/0031-9155/39/i=3/a=001. [PubMed: 15551582]

El Fakhri G, Surti S, Trott CM, Scheuermann J, Karp J. Improvement in lesion detection with whole-body oncologic time-of-flight pet. Journal of Nuclear Medicine. 2011; 52(3):347–353. [PubMed: 21321265]

Fessler, JA. Analytical approach to regularization design for isotropic spatial resolution. Nuclear Science Symposium Conference Record, 2003 IEEE; IEEE; 2003. p. 2022-2026.

Fessler J, Rogers W. Spatial resolution properties of penalized-likelihood image reconstruction: space-invariant tomographs. Image Processing, IEEE Transactions on. 1996; 5(9):1346–1358.

Frese T, Rouze N, Bouman C, Sauer K, Hutchins G. Quantitative comparison of fbp, em, and bayesian reconstruction algorithms for the indypet scanner. Medical Imaging, IEEE Transactions on. 2003; 22(2):258–276.

Gariod, R.; Allemand, R.; Cormoreche, E.; Laval, M.; Moszynski, M. The leti positron tomograph architecture and time of flight improvements. Proceedings of The Workshop on Time of Flight Tomography; 1982. p. 25-29.

Hong I, Chung S, Kim H, Kim Y, Son Y, Cho Z. Ultra fast symmetry and simd-based projection-backprojection (ssp) algorithm for 3-d pet image reconstruction. Medical Imaging, IEEE Transactions on. 2007; 26(6):789–803.

Jakoby BW, Bercier Y, Conti M, Casey ME, Bendriem B, Townsend DW. Physical and clinical performance of the mct time-of-flight pet/ct scanner. Physics in Medicine and Biology. 2011; 56(8):2375. URL: http://stacks.iop.org/0031-9155/56/i=8/a=004. [PubMed: 21427485]

Kadrmas DJ, Casey ME, Conti M, Jakoby BW, Lois C, Townsend DW. Impact of time-of-flight on pet tumor detection. Journal of Nuclear Medicine. 2009; 50(8):1315–1323. [PubMed: 19617317]

Karp J, Surti S, Daube-Witherspoon M, Muehllehner G. Benefit of time-of-flight in pet: Experimental and clinical results. J Nucl Med. 2008; 49:462–470. [PubMed: 18287269]

Kinahan, P.; Michel, C.; Defrise, M.; Townsend, D.; Sibomana, M.; Lonneux, M.; Newport, D.; Luketich, J. Fast iterative image reconstruction of 3d pet data. Nuclear Science Symposium, 1996. Conference Record., 1996 IEEE; 1996. p. 1918-1922.

Li, Q.; Bai, B.; Cho, S.; Smith, A.; Leahy, R. Count independent resolution and its calibraion. Proceedings of 10th International Meeting on Fully Three-Dimensional Image Reconstruction in Radiology and Nuclear Medicine; 2009. p. 223-226.

Lin, Y.; Bai, B.; Zhou, W.; Ren, R.; Li, Q.; Dahlbom, M.; DiFilippo, F.; Leahy, RM. Optimized map reconstruction of h2-weighted fourier rebinned tof pet. The 12th International Meeting on Fully Three-Dimensional Image Reconstruction in Radiology and Nuclear Medicine; 2013. p. 292-295.

Lin, Y.; Li, Q.; Leahy, RM. Fast gpu-based time-of-flight map reconstruction with a factored system matrix. Nuclear Science Symposium Conference Record (NSS/MIC), 2010 IEEE; IEEE; 2010. p. 2889-2893.

Liu X, Comtat C, Michel C, Kinahan P, Defrise M, Townsend D. Comparison of 3-d reconstruction with 3d-osem and with fore+ osem for pet. Medical Imaging, IEEE Transactions on. 2001; 20(8): 804–814.

Moses W, Derenzo S. Prospects for time-of-flight pet using lso scintillator. Nuclear Science, IEEE Transactions on. 1999; 46(3):474–478.

Ollinger J, Fessler J. Positron-emission tomography. Signal Processing Magazine, IEEE. 1997; 14(1): 43–55.

Pratx G, Chinn G, Olcott PD, Levin CS. Fast, accurate and shift-varying line projections for iterative reconstruction using the gpu. Medical Imaging, IEEE Transactions on. 2009; 28(3):435–445.

Qi J, Leahy R, Cherry S, Chatziioannou A, Farquhar T. High-resolution 3d bayesian image reconstruction using the micropet small-animal scanner. Physics in Medicine and Biology. 1998b; 43(4):1001. URL: http://stacks.iop.org/0031-9155/43/i=4/a=027. [PubMed: 9572523]

Qi J, Leahy R, Hsu C, Farquhar T, Cherry S. Fully 3d bayesian image reconstruction for the ecat exact hr+ Nuclear Science, IEEE Transactions on. 1998a; 45(3):1096–1103.

Qi J, Leahy RM. Resolution and noise properties of map reconstruction for fully 3-d pet. Medical Imaging, IEEE Transactions on. 2000; 19(5):493–506.

Stayman JW, Fessler JA. Regularization for uniform spatial resolution properties in penalized-likelihood image reconstruction. Medical Imaging, IEEE Transactions on. 2000; 19(6):601–615.

Tohme MS, Qi J. Iterative reconstruction of fourier-rebinned pet data using sinogram blurring function estimated from point source scans. Medical physics. 2010; 37:5530. [PubMed: 21089788]

Tomitani T. Image reconstruction and noise evaluation in photon time-of-flight assisted positron emission tomography. Nuclear Science, IEEE Transactions on. 1981; 28(6):4581–4589.

Vunckx K, Zhou L, Matej S, Defrise M, Nuyts J. Fisher information-based evaluation of image quality for time-of-flight pet. Medical Imaging, IEEE Transactions on. 2010; 29(2):311–321.

Wang, W.; Hu, Z.; Gualtieri, E.; Parma, M.; Walsh, ES.; Sebok, D.; Hsieh, YL.; Tung, CH.; Song, X.; Griesmer, J.; Kolthammer, JA.; Popescu, LM.; Werner, M.; Karp, JS.; Gagnon, D. Systematic and distributed time-of-flight list mode pet reconstruction. Nuclear Science Symposium Conference Record, 2006 IEEE; 2006. p. 1715-1722.

Watson CC. An evaluation of image noise variance for time-of-flight pet. Nuclear Science, IEEE Transactions on. 2007; 54(5):1639–1647.

Wong WH, Mullani NA, Philippe EA, Hartz R, Gould KL, et al. Image improvement and design optimization of the time-of-flight pet. Journal of nuclear medicine: official publication, Society of Nuclear Medicine. 1983; 24(1):52.

Yamamoto M, Ficke DC, Ter-Pogossian MM. Experimental assessment of the gain achieved by the utilization of time-of-flight information in a positron emission tomograph (super pett i). Medical Imaging, IEEE Transactions on. 1982; 1(3):187–192.

Zhou J, Qi J. Fast and efficient fully 3d pet image reconstruction using sparse system matrix factorization with gpu acceleration. Physics in Medicine and Biology. 2011; 56(20):6739. [PubMed: 21970864]

7. Appendix

Here we derive the relationships between the mean and variance of the FORET-2D and FORET-3D rebinned data summarized in (12). As illustrated in Figure 1, we apply a sequence of operations to convert the data from 3D TOF to rebinned 2D or 3D nonTOF sinograms. Each of these steps affects the variance of the processed data. In the final step we perform an affine transform on each sample so that the variance and mean are approximately equal and we can apply a MAP reconstruction method based on a Poisson likelihood model.

7.1. The Effect of Data Correction and Arc Correction on Variance

After normalization, attenuation correction, scatter and random correction the corrected data have the form:

$$\mathbf{y}_c^{TOF} = \mathbf{P}_{norm}^{TOF^{-1}} \mathbf{P}_{attn}^{TOF^{-1}} (\mathbf{y}^{TOF} - \widehat{\mathbf{r}}^{TOF} - \widehat{\mathbf{s}}^{TOF}) \quad (21)$$

Assuming that $\mathbf{P}_{blur}^{TOF^{-1}}$ and $\mathbf{P}_{attn}^{TOF^{-1}}$ are commutative, using (7), (8) and the fact that (i) each term on the right hand side of (7) is independent, and (ii) multiplication of a random variable with a constant scales its variance by the square of that constant, we have:

$$var(\mathbf{y}_c^{TOF}) \approx \mathbf{P}_{norm}^{TOF^{-1}} \mathbf{P}_{attn}^{TOF^{-1}} \mathbf{P}_{blur}^{TOF} \mathbf{P}_{geom}^{TOF} \mathbf{x} + \mathbf{P}_{norm}^{TOF^{-2}} \mathbf{P}_{attn}^{TOF^{-2}} (\bar{\mathbf{r}}^{TOF} + \bar{\mathbf{s}}^{TOF}) \quad (22)$$

The next step of arc correction is implemented using linear interpolation with each resampled data point formed as a weighted sum of its two nearest neighbors, which can be represented in matrix form as:

$$\mathbf{y}_{arc}^{TOF} = \mathbf{M}_{arc} \mathbf{y}_c^{TOF} \quad (23)$$

with covariance:

$$cov(\mathbf{y}_{arc}^{TOF}) = \mathbf{M}_{arc}\, cov(\mathbf{y}_c^{TOF}) \mathbf{M}_{arc}^T \quad (24)$$

Note that the corrected data in (21) are independent and matrix $\mathbf{M}_{arc}$ has at most two nonzero entries per row. If the variance of the data varies relatively slowly between adjacent radial samples, we can approximate the diagonal elements of the covariance to give the following expression for the variance of the arc corrected data:

$$var(\mathbf{y}_{arc}^{TOF}) = \mathbf{C}_{arc}\, var(\mathbf{y}_c^{TOF}) \quad (25)$$

where $\mathbf{C}_{arc}$ is a diagonal matrix whose i^{th} diagonal element equals the i^{th} diagonal element of $\mathbf{M}_{arc}\mathbf{M}_{arc}^{T}$. Figure 16 shows a plot of the diagonal elements of $\mathbf{C}_{arc}$ as a function of radial coordinate. Note that variance scaling varies between 1 (when a single sample is used for arc correction) and 0.5 when two samples are used with equal weight. We use a similar approach for un-arc correction resulting in the corresponding variance scaling after rebinning with $\mathbf{C}_{unarc}$.

7.2. The Effect of Rebinning on Variance

Having developed expressions for the effects of data correction and arc and un-arc corrections, it remains to find approximate expressions for the variance reduction effect resulting from rebinning to 2D or 3D nonTOF formats. For this development we will return to a continuous representation of the data so we can make use of the Fourier transform relationships that underlie FORET. We presented the variance scaling in a common framework for 2D and 3D FORET in the body of the paper, but at this point we need to consider the two methods separately.

Variance properties for FORET-3D have already been extensively studied in an earlier paper (Ahn et al. 2011), which showed that the variance of 3D PET data rebinned using FORET-3D was related to that of 3D PET data formed by simply summing over time of flight bins by a simple scalar factor:

$$K_{F3D}=\frac{1}{\sum_{\omega_t}\mathscr{H}^2(\omega_t)} \quad (26)$$

assuming that an optimal weighting $\alpha(\omega_t) = H^2(\omega_t)$ is used.

The case for FORET-2D is more complicated as we also need to consider the impact of spatial rebinning from 3D to 2D. Here we adapt the variance estimation method initally proposed in (Comtat et al. 1998) to the TOF case. Making the simplifying assumption that $\omega_s^{'}=\omega_s$, as in the original FORET-2D method (Cho et al. 2009), we can rewrite the rebinning equation (6) as

$$\begin{aligned}\mathscr{P}_{FT}^{2D}(\omega_s,k,z)&=\mathscr{P}(\omega_s,k,z,0;0)\\&=\sum_{z',\delta,\omega_t}\mathscr{A}_{2D}(\omega_s,k,z,z',\delta;\omega_t)\mathscr{P}(\omega_s,k,z',\delta;\omega_t)\end{aligned} \quad (27)$$

where $\mathscr{A}_{2D}(\omega_s, k, z, z', \delta; \omega_t)$ represents the coefficients in (6).

Take the 2D inverse FT of (27) with respect to ω_s and k and applying Parseval's theorem (N_t $\Sigma_t x(t)y(t) = \Sigma_{\omega_t}X^*(\omega_t)Y(\omega_t)$) with respect to ω_t:

$$p_{FT}^{2D}(s,\phi,z)=N_t\sum_{s',\phi',z',\delta;t}[a_{2D}(s-s',\phi-\phi',z,z',\delta;-t)p^{TOF}(s',\phi',z',\delta;t)] \quad (28)$$

where a_{2D} is the 2D inverse FT of $\mathscr{A}_{2D}$ with respect to ω_s and k.

Note that $a_{2D}(s, \varphi, z, z', \delta; t)$ is a convolutional kernel in (s, φ) which can be computed by applying FORET-2D to an impulse sinogram $\delta(0, 0, z', \delta; t)$ for each value of (z', δ, t). Under the assumption that the data are uncorrelated, the variance of the FORET-2D rebinned data can be expressed as:

$$var(p_{FT}^{2D}(s,\phi,z)) \approx N_t^2 \sum_{s',\phi',z',\delta,t} [a_{2D}^2(s-s',\phi-\phi',z,z',\delta;-t) var(p^{TOF}(s',\phi',z',\delta;t)) \quad (29)$$

Equation (29) can be further simplified by assuming the contribution of each *t* component can be approximated by the average over *t*:

$$\begin{aligned} var(p_{FT}^{2D}(s,\phi,z)) &\approx N_t^2 \sum_{s',\phi',z',\delta,t} [a_{2D}^2(s-s',\phi-\phi',z,z',\delta;-t) \frac{\sum_{t'} var(p^{TOF}(s',\phi',z',\delta;t'))}{N_t} \\ &\approx N_t \sum_{s',\phi',z',\delta} [var(p^{3D}(s',\phi',z',\delta)) \sum_t a_{2D}^2(s-s',\phi-\phi',z,z',\delta;-t)] \end{aligned} \quad (30)$$

Similarly, we assume that for each slice z, we can approximate the variance for all oblique angles as the average over those angles for each z. This is equivalent to performing a single slice rebinning (SSRB) of the variances, as originally proposed by (Comtat et al. 1998):

$$var(p_{FT}^{2D}(s,\phi,z)) \approx N_t \sum_{s',\phi'} V_{SSRB}(s',\phi',z) k_{2D}(s-s',\phi-\phi',z) \quad (31)$$

where $V_{SSRB}(s, \varphi, z)$ is the SSRB of the nonTOF data variance:

$$V_{SSRB}(s,\phi,z) = \frac{\sum_{z',\delta} \delta(z',z) var(p^{3D}(s,\phi,z',\delta))}{\sum_{z',\delta} \delta(z',z)} \quad (32)$$

with $\delta(z', z)$ the Kronecker delta and

$$k_{2D}(s,\phi,z) = \sum_{z',\delta,t} a_{2D}^2(s,\phi,z,z',\delta;t) \quad (33)$$

computed as the appropriate sum over the FORET-2D rebinnings of the impulse sinograms described above.

Finally, we note that $a(s, \varphi, z, z', \delta; t)$ is highly localized near the origin in *s* and φ and therefore so is $k(s, \varphi, z)$. To illustrate this property, we show in Figure 17 an image of $k_{2D}(s, \varphi, z)$ for the plane at axial center of the scanner. Using this property, we can approximate (31) as:

$$var(p_{FT}^{2D}(s,\phi,z)) = K_{F2D}(z) V_{SSRB}(s,\delta,z) \quad (34)$$

where $K_{2D}(z)$ is the slice variance reduction factor:

$$K_{F2D}(z) = N_t \sum_{s,\phi} k_{2D}(s,\phi,z) \quad (35)$$

7.3. The Full Variance Model

Having developed expressions for the variance scaling effects of each step in Fig. 1 we now assemble them into a full model that we use as the basis for scaling of the rebinned un-arc corrected data to achieve a quasi-Poisson distribution. The full effects of the complete

rebinning chain on variance are obtained by combining models of data correction (22), arc and un-arc correction (25), and FORET-3D (26) or FORET-2D (34).

The expression for the final variance for FORET-3D can be written as:

$$var(\mathbf{y}_{unarc}^{FORET3D}) = \mathbf{K}_{FORET}^{3D}\mathbf{P}_{norm}^{3D\ -1}\mathbf{P}_{attn}^{3D\ -1}\bar{\mathbf{y}}_{unarc}^{FORET3D} + \hat{\mathbf{r}}^{FORET3D} \quad (36)$$

where $\bar{\mathbf{y}}_{unarc}^{FORET3D}$ is the mean value of the un-arc corrected rebinned nonTOF 3D data and

$$\mathbf{K}_{FORET}^{3D} = K_{F3D}\mathbf{C}_{unarc}^{3D}\mathbf{C}_{arc}^{3D} \quad (37)$$

with K_{F3D} defined in (26). The effect on variance of randoms and scatter subtraction can be modeled as:

$$\hat{\mathbf{r}}^{FORET3D} = K_{F3D}\mathbf{C}_{unarc}^{3D}\mathbf{C}_{arc}^{3D}\mathbf{P}_{norm}^{3D\ -2}\mathbf{P}_{attn}^{3D\ -2}(\bar{\mathbf{r}}^{3D} + \bar{\mathbf{s}}^{3D}) \quad (38)$$

where $\mathbf{r}^{3D}$ and $\mathbf{s}^{3D}$ are the sinograms formed by applying FORET-3D to the mean (or estimated) randoms and scatter contributions to the prompt counts.

Similarly, the expression for the final variance for FORET-2D can be written as:

$$var(\mathbf{y}_{unarc}^{FORET2D}) = \mathbf{K}^{2D}SSRB(\mathbf{C}_{arc}^{3D}\mathbf{P}_{norm}^{3D\ -1}\mathbf{P}_{attn}^{3D\ -1}\mathbf{P}_{blur}^{3D}\mathbf{P}_{geom}^{3D}\mathbf{x}) + \hat{\mathbf{r}}^{FORET2D} \quad (39)$$

where

$$\hat{\mathbf{r}}^{FORET2D} = \mathbf{K}^{2D}SSRB[\mathbf{C}_{arc}^{3D}\mathbf{P}_{norm}^{3D\ -2}\mathbf{P}_{attn}^{3D\ -2}(\bar{\mathbf{r}}^{3D} + \bar{\mathbf{s}}^{3D})] \quad (40)$$

and

$$\mathbf{K}^{2D} = (D(K_{F2D}) \otimes I_{N_s \times N_\phi})\mathbf{C}_{unarc}^{2D} \quad (41)$$

with $D(K_{F2D})$ an $N_{p2d} \times N_{p2d}$ diagonal matrix with $D(i, i) = K_{F2D}(i)$;N_s and N_φ are the number of samples of s and φ respectively, and N_{p2d} is the number of 2D sinograms.

In (39) we compute the single slice rebinning variance component of variance reduction using the variance weightings due to normalization, attentuation correction and arc correction performed in the 3D space. This then requires that we perform both FORET-2D and FORET-3D in order to compute variance estimates for the 2D case. An alternative additional simplification is as follows. We can assume that in a clinical scanner, oblique angles are small and that variations in attenuation and normalization can be ignored when rebinning. In that case we can simplify the model of the effect on variance of single slice rebinning as follows:

$$\begin{aligned} SSRB(\mathbf{C}_{arc}^{3D}\mathbf{P}_{norm}^{3D\ -1}\mathbf{P}_{attn}^{3D\ -1}\mathbf{P}_{blur}^{3D}\mathbf{P}_{geom}^{3D}\mathbf{x}] &\approx \mathbf{C}_{arc}^{2D}\mathbf{P}_{norm}^{2D\ -1}\mathbf{P}_{attn}^{2D\ -1}SSRB(\mathbf{P}_{blur}^{3D}\mathbf{P}_{geom}^{3D}\mathbf{x}) \\ &\approx \mathbf{C}_{arc}^{2D}\mathbf{P}_{norm}^{2D\ -1}\mathbf{P}_{attn}^{2D\ -1}\mathbf{P}_{blur}^{2D}\mathbf{P}_{geom}^{2D}\mathbf{x} \\ &\approx \mathbf{C}_{arc}^{2D}\mathbf{P}_{norm}^{2D\ -1}\mathbf{P}_{attn}^{2D\ -1}\bar{\mathbf{y}}_{unarc}^{FORET2D} \end{aligned} \quad (42)$$

As a result we do not need to perform single slice rebinning of the 3D data but instead compute the variance estimate as:

$$var(\mathbf{y}_{unarc}^{FORET2D}) \approx \mathbf{K}^{2D}\mathbf{C}_{arc}^{2D}\mathbf{P}_{norm2d}^{2D\ -1}\mathbf{P}_{attn}^{2D\ -1}\bar{\mathbf{y}}_{unarc}^{FORET2D}+\hat{\mathbf{r}}^{FORET2D} \quad (43)$$

In Figure 17 presented in the body of the paper we compared the two approximations (43) and (39) as justification for using the simpler expression for the remainder of our studies.

In conclusion, in this appendix we have derived approximate expressions (43) and (36) for the variance of FORET 2D and 3D rebinned data which we can express in the common form:

$$var(\mathbf{y}_{unarc}^{FORET})=\mathbf{G}\bar{\mathbf{y}}_{unarc}^{FORET}+\mathbf{L}(\bar{\mathbf{r}}^{3D}+\bar{\mathbf{s}}^{3D}) \quad (44)$$

where $\mathbf{y}_{unarc}^{FORET}$ is the mean of the unarc corrected 2D or 3D FORET rebinned data, $\mathbf{r}^{3D}$ and $\mathbf{s}^{3D}$ are respectively the 3D estimates of randoms and scatter, and **G** and **L** are respectively matrices combining all terms that affect the variance of the final rebinned data. **G** is a diagonal matrix. **L** is diagonal for FORET-3D but not for FORET-2D since it involves the SSRB of the data variance. In Section 4.2 we use these expressions to develop a scaling of the rebinned data so that the resulting data is quasi-Poisson, i.e. their mean and variances match.

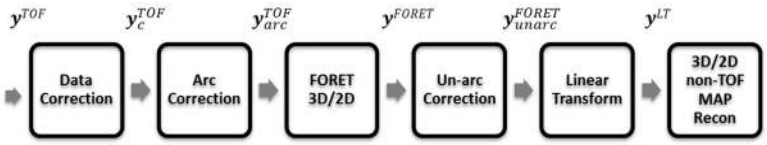

Figure 1.
Flow chart for MAP reconstruction using FORET rebinned data.

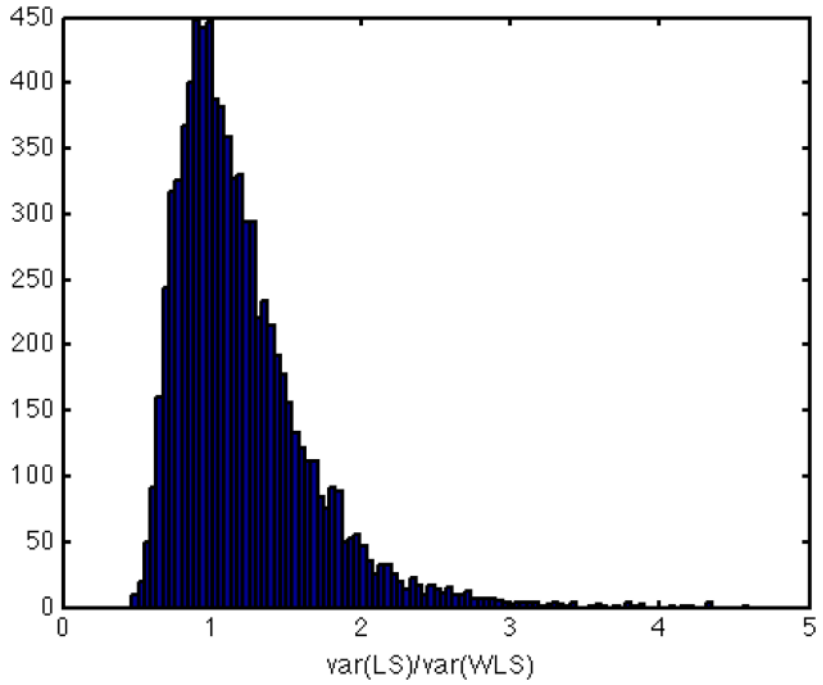

Figure 2.
Histogram of the ratio of the variance of the unweighted LS and diagonal WLS solutions.

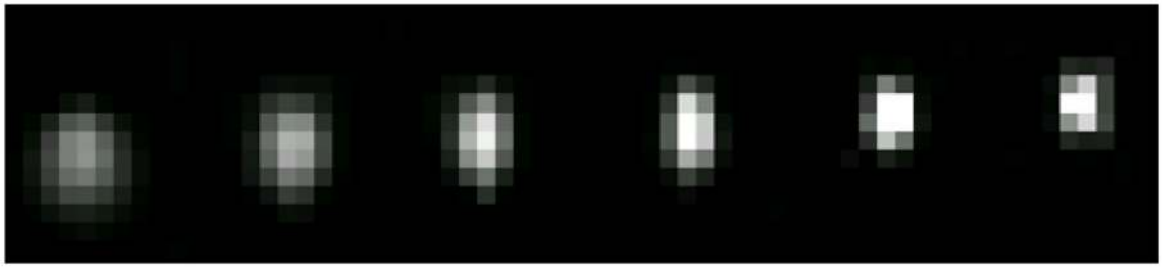

Figure 3.
Sample blur kernel used for FORET-3D rebinned data, from left to right: larger radial displacement to smaller radial displacement.

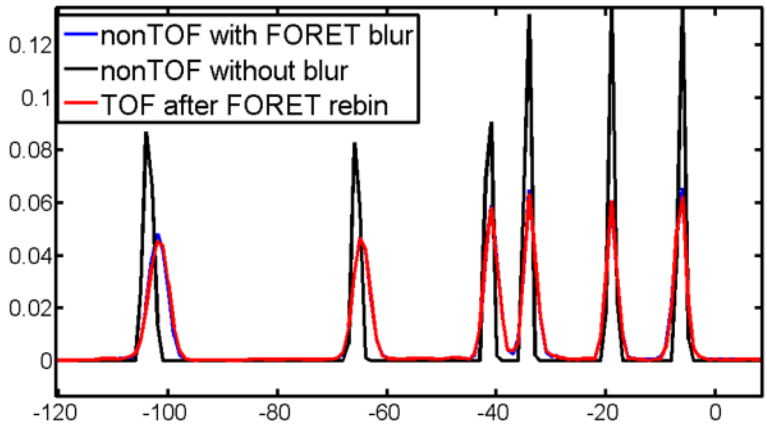

Figure 4.
Profiles of selected point source sinograms, from left to right: larger radial displacement to smaller radial displacement. 0 represents the center of the scanner.

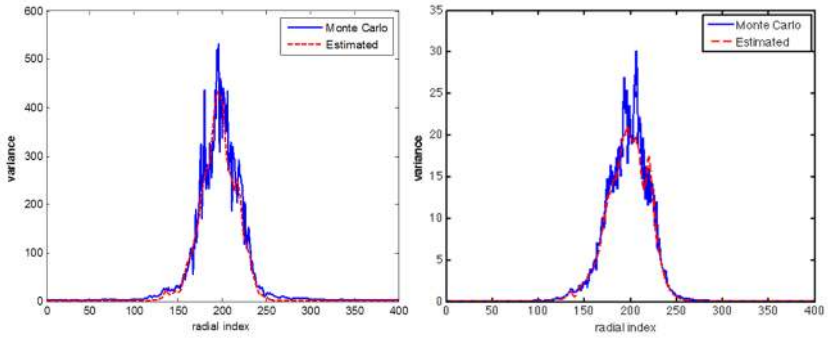

Figure 5.
Comparison of sample variance from Monte Carlo simulation and estimated from (12), angle index=100, sinogram index=5. Left: FORET-3D, Right: FORET-2D.

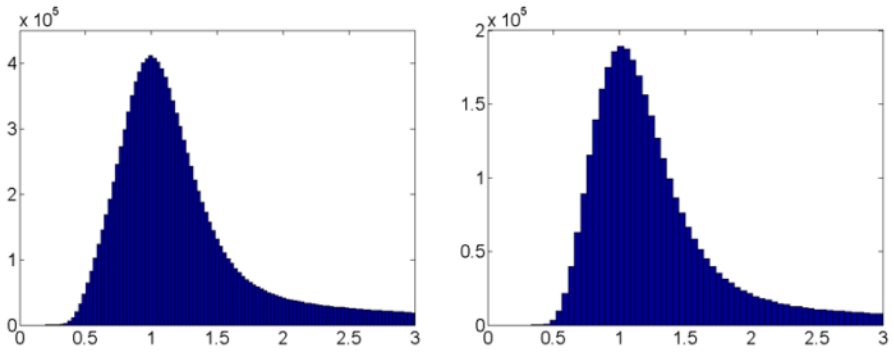

Figure 6.
Histogram of variance to mean ratios of FORET after the affine transform in (13) at which point the mean and variance should be equal. Only the sinogram elements within the object region was plotted. Left: FORET-3D, Right: FORET-2D. The modes are 0.995 for FORET-3D and 1.01 for FORET-2D

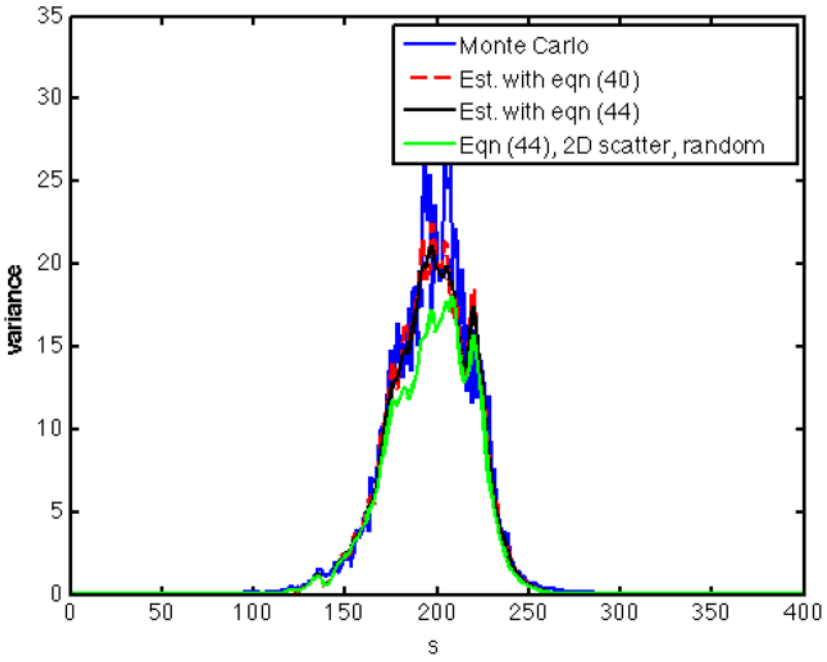

Figure 7.
Comparison of different approximations for computing variance in FORET-2D. See text for explanation.

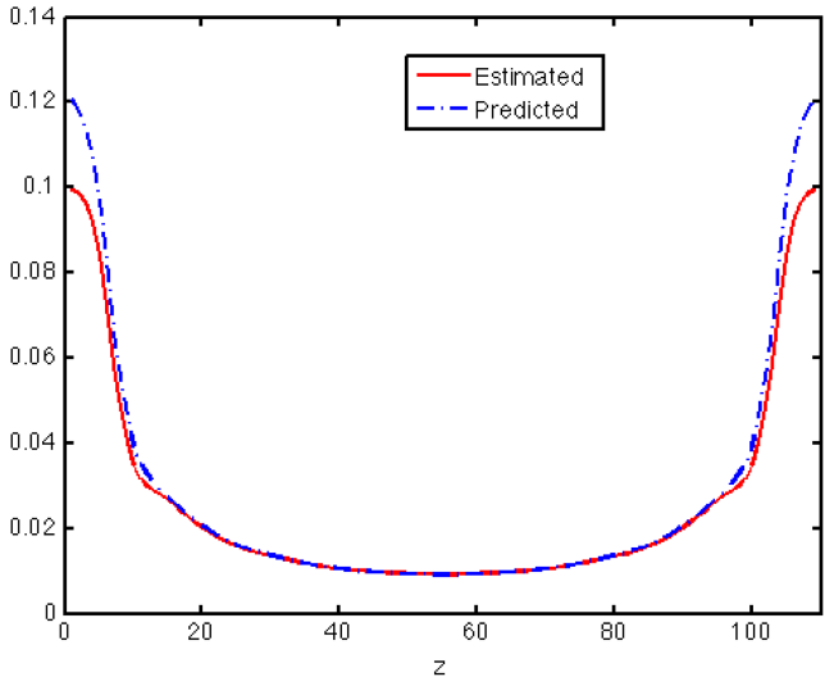

Figure 8.
Variance reduction factor $K_{F2D}(z)$ (see Appendix, (35)) for FORET-2D as a function of axial position compared to variance reduction calculated by Monte Carlo simulation.

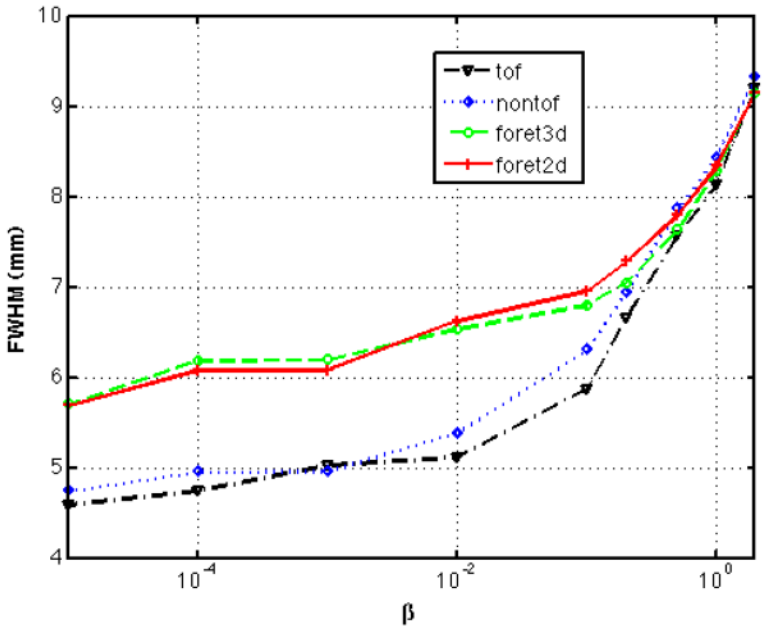

Figure 9.
Resolution vs. β calibration table generated from simulated point source data for the Siemens mCT scanner for each of the four different data representations used in subsequent studies.

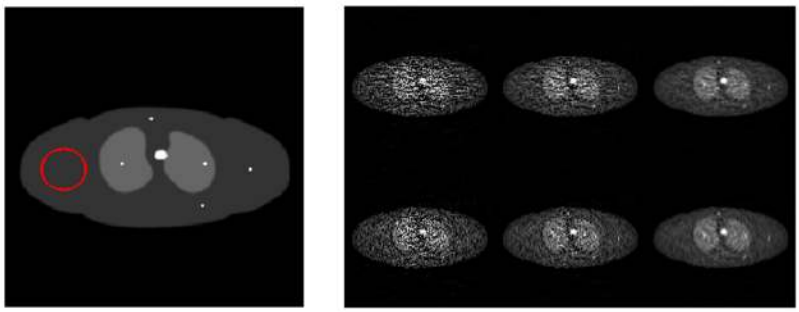

Figure 10.

Left: true phantom. Right: Reconstructed images. Images in the top row are reconstructed from FORET rebinned sinogram directly. Images in the bottom row are from rescaled data using accurate mean and variance of the rebinned data and quasi-Poisson noise model. From left to right the target resolution are 6mm, 7mm and 8mm respectively. The red circle indicates the ROI used for noise measurements

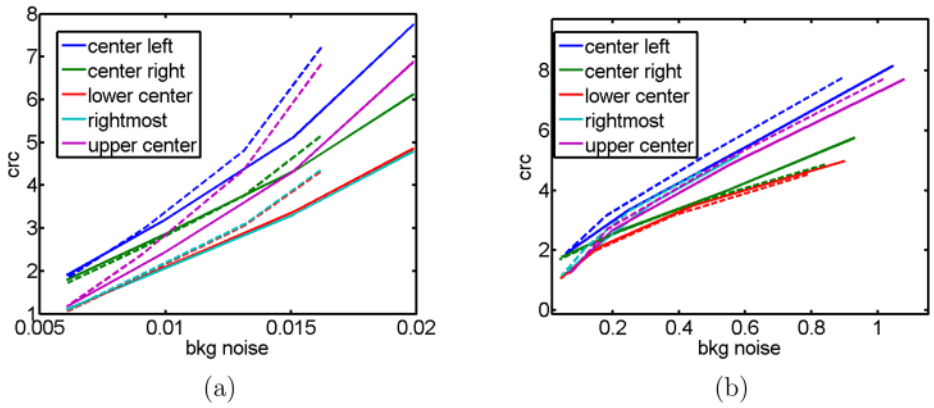

Figure 11.
CRC vs. noise. (a) Noise measured using variance of the mean of ROI from Monte Carlo simulation; (b) noise measured using ROI variance from one sample reconstruction. Dashed curves are from rescaled data using accurate mean and variance of rebinned data, solid curves are from rebinned data directly.

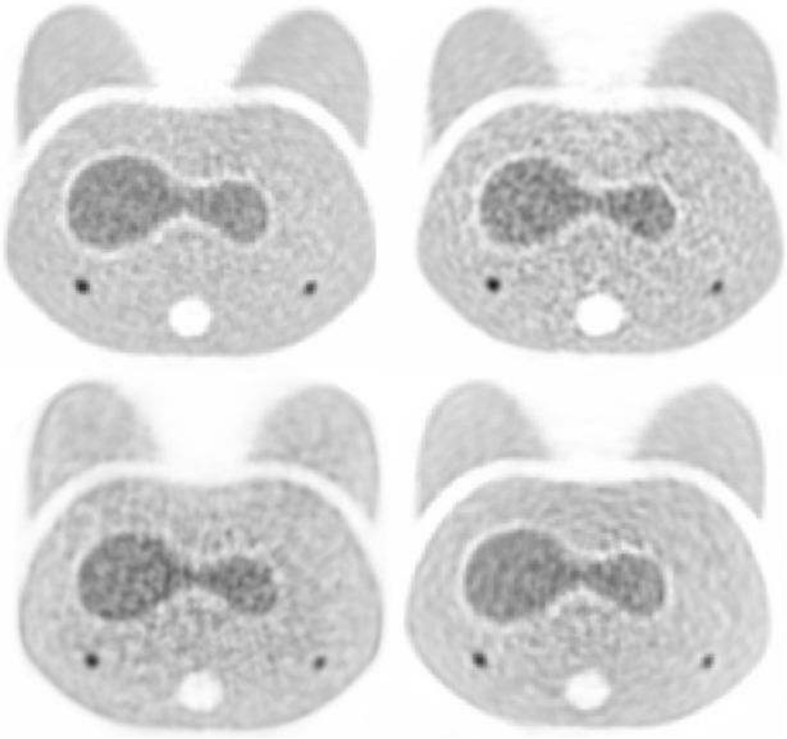

Figure 12.
Sample reconstructed phantom images using different data formats. Upper left: TOF, upper right: nonTOF, lower left: FORET-2D, lower right: FORET-3D.

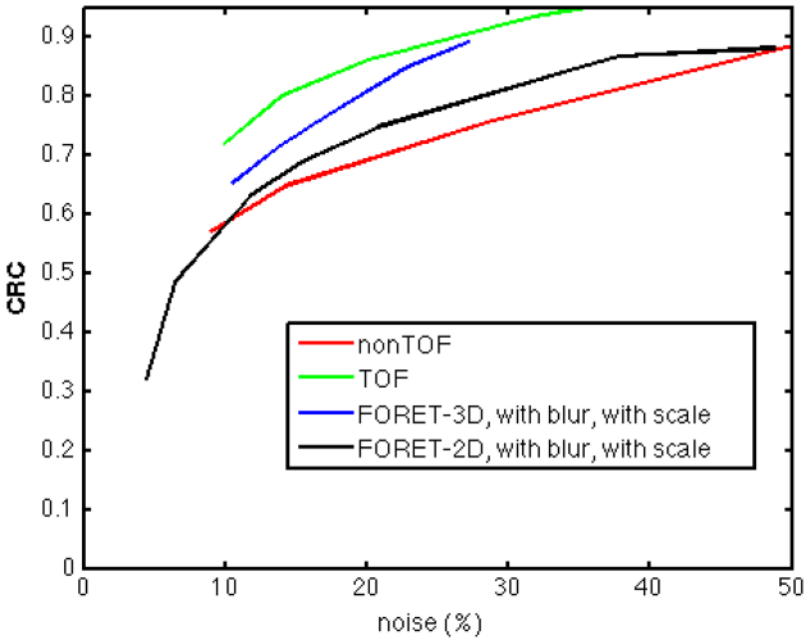

Figure 13.
CRC vs. noise curves of images reconstructed from TOF, nonTOF, FORET-3D and FORET-2D data.

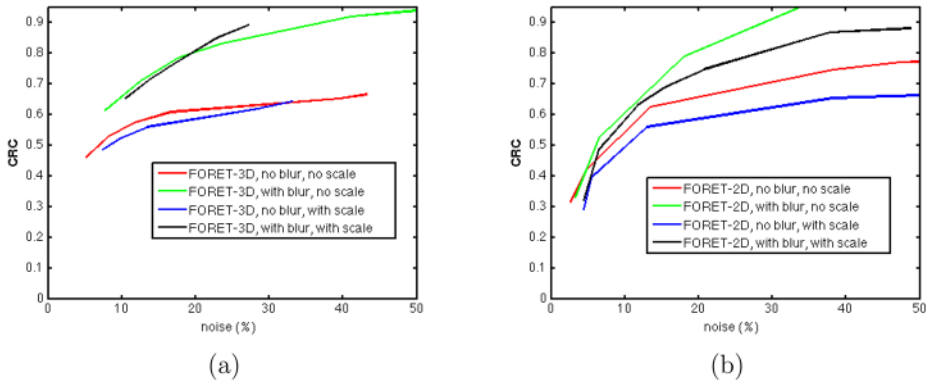

Figure 14.
CRC vs. noise curves of images reconstructed from (a) FORET-3D; (b) FORET-2D.

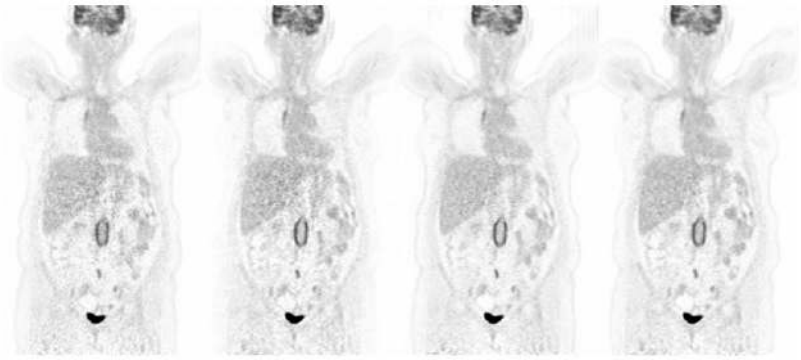

Figure 15.
Comparison of whole-body patient images. From left to right: nonTOF, FORET-2D, FORET-3D, TOF. All images have resolution of 6mm.

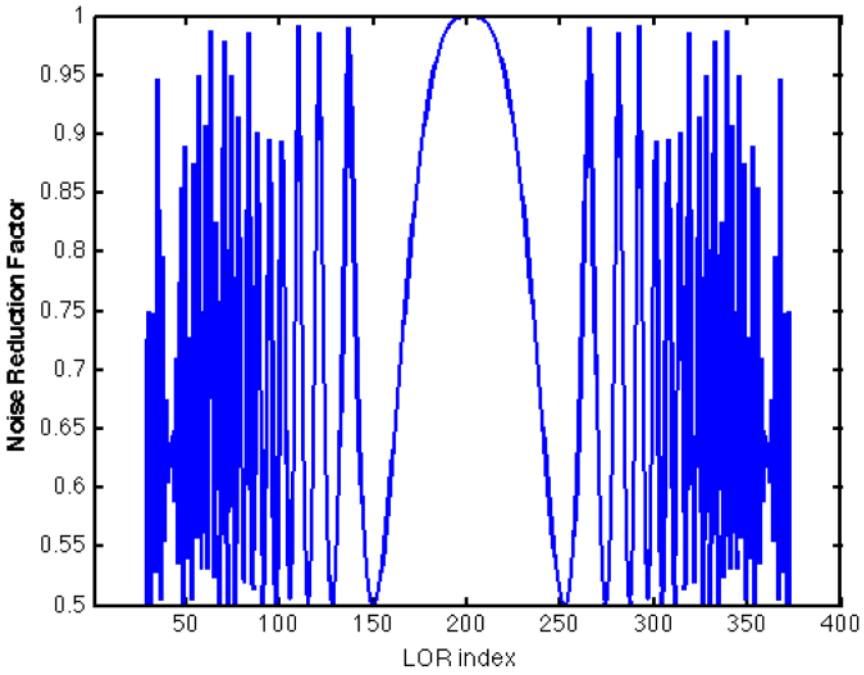

Figure 16.
Noise reduction factors due to arc correction.

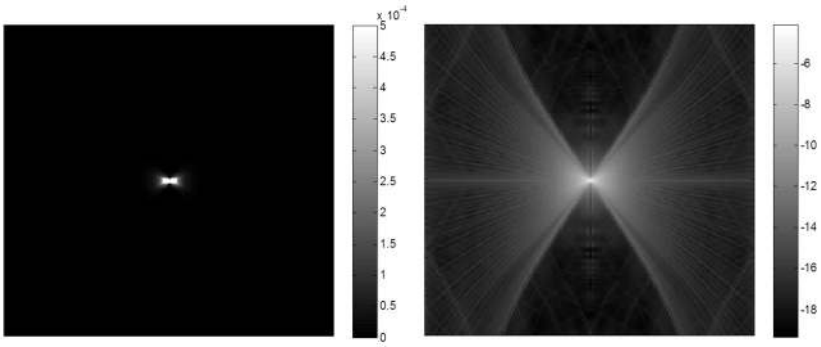

Figure 17.

$K_{2D}(s, \varphi, z)$ for the central slice in the scanner shown in linear (left) and log scale (right). Horizontal axis: angle, φ; vertical axis: radial coordinate, s.

Table 1

Computation Time for FORET rebinning and MAP Reconstruction (1 iteration)

FORET2D rebinning	FORET3D rebinning	MAP2D nonTOF	MAP 3D nonTOF	MAP 3D TOF
1.3 min	1.6 min	0.3 min	2.4 min	12.6 min

Table 2

Simulated 3D TOF PET System Parameters

Parameter	Value
Number of detectors	672
Number of rays (LORs) per angle	400
Radius of detector ring	427.6
Detector Z size (mm)	4.00
Number of rings	55
Max ring difference	49
Span	11
Image size	256×256×109
Image transverse voxel size (mm)	2.025
Number of TOF bins	15
TOF time resolution (mm)	82.54
TOF bin spacing (mm)	46.8

Table 3

Mean Noise Measurement in Patient Image

Method	Mean	SD	%SD
TOF	0.5770.570	0.1090.0796	18.914.0
FORET-3D	0.5690.573	0.1100.0884	19.315.4
FORET-2D	0.6170.575	0.1510.107	24.518.6
nonTOF	0.5680.593	0.1550.124	27.320.9